

# We are IntechOpen, the world's leading publisher of Open Access books Built by scientists, for scientists

6,900

Open access books available

185,000

International authors and editors

200M

Downloads

Our authors are among the

154

Countries delivered to

TOP 1%

most cited scientists

12.2%

Contributors from top 500 universities



WEB OF SCIENCE™

Selection of our books indexed in the Book Citation Index  
in Web of Science™ Core Collection (BKCI)

Interested in publishing with us?  
Contact [book.department@intechopen.com](mailto:book.department@intechopen.com)

Numbers displayed above are based on latest data collected.  
For more information visit [www.intechopen.com](http://www.intechopen.com)



---

# Ag-Cu Nanoalloys as Oxygen Reduction Electrocatalysts in Alkaline Media for Advanced Energy Conversion and Storage

---

Adnan Qaseem, Fuyi Chen and Nan Zhang

Additional information is available at the end of the chapter

<http://dx.doi.org/10.5772/62050>

---

## Abstract

Silver-based nanoalloys owing to their cost, performance and stability are an attractive electrocatalyst system for oxygen reduction reaction (ORR) in the alkaline fuel cells and metal air batteries. A systematic computational and experimental approach has been adopted to investigate their performance for ORR in alkaline environment. Firstly, genetic algorithm (GA) based calculations have been performed to look for the stable compositions and structures of these nanoalloys. Later, density functional theory (DFT) is employed to simulate the working of those stable nanoalloys in actual working conditions. Finally, the most promising nanoalloys have been synthesized by physical and chemical routes to confirm their performance in real-life conditions. It has been found that the alloying of silver with copper enhances the catalytic performance of Ag nanoparticles. The enhancement in performance can be related to the modification of the electronic and physical structure of Ag due to copper doping. The superior performance of Ag-Cu nanocatalysts in alkaline fuel cells and metal air batteries along with their modest cost and long-term stability make them a promising candidate for deployment as a catalyst for ORR in alkaline media.

**Keywords:** Electrocatalyst, silver nanoalloys, metal air batteries, oxygen reduction reaction, rechargeable zinc air battery

---

## 1. Introduction

Oxygen reduction reaction (ORR) plays a vital role in the working of fuel cells and metal-air batteries. Both of these technologies utilize oxygen from the air to generate electrical energy. The ORR mechanism in acidic environment is accompanied with the formation of water.

---



For alkaline medium, hydroxyl formation takes place as



The current Li-ion battery technology is unable to offer the solutions for the long-range electric vehicles and energy storage grids. It is also postulated that the Li-ion battery system may reach its theoretical limit which will still be short of the demand for the long-range EVs. Metal air batteries such as Li-air (11,000 Wh/kg) and Zn-air systems (1,084 Wh/kg) offer much higher energy capacities [1–3]. A great deal of contemporary research is directed toward the realization of these high energy systems. Apart from being dense in energy, metal air batteries and fuel cells are green source of energy. The product of their working is free from toxic and harmful waste gases which damage the environment. These systems provide a valuable opportunity to cut the greenhouse gas emissions on a tremendous scale [4,5].

Electrocatalyst plays a crucial role in the working of metal air batteries and fuel cells. The ORR and OER mechanism are strongly related to the functionality of the electrocatalyst. Pt and Pt-based alloy catalysts are widely used for ORR, but prohibitive cost and catalytic poisoning are major drawbacks associated with Pt. Therefore, it is highly desirable to explore novel Pt-free cost-effective catalysts. Different non-platinum catalysts have been considered as a replacement of Pt. Silver being about 50 times cheaper than platinum is an attractive choice for catalyst in alkaline fuel cells. The pourbaix diagram reveals the superior stability of Ag over platinum in alkaline environment [6,7].

The ORR is accompanied with the formation of various adsorbed intermediates such as O, OH and OOH. Norkosov et al. evaluated the effect of potential on the free energy of various intermediates on Pt (111) by DFT calculations [8]. At high potential, the adsorbed oxygen was found to be stable. The ORR reaction was found to proceed only by lowering the potential, hence giving rise to overpotential. Bond energies of oxygen and hydroxyl on different metals were also calculated by DFT. The rate of ORR is limited by the removal of O, OH for metals which bind oxygen strongly where as in case of metals with poor oxygen binding, the rate is limited by the weak bonding of the adsorbed species. A volcano plot as shown in Figure 1 is obtained as a result of DFT calculations performed on various systems. Although platinum sits near the top of volcano plot developed by DFT calculations, alloying of metals can result in new materials with adsorption energies for the intermediates that are different from the constituent pure metals. Therefore, new generation of superior electrocatalysts can be developed by alloying of metals to yield optimum binding of adsorbates onto alloy surface.

Tremendous amount of research has been performed in the past decade to enhance the activity of ORR catalyst. A myriad of bimetallic and multi metallic alloy compositions have been developed in a variety of structures such as core shell, skin alloys, thin films, ordered intermetallics and solid solutions [9–12]. Skin alloys have been widely popular because of their

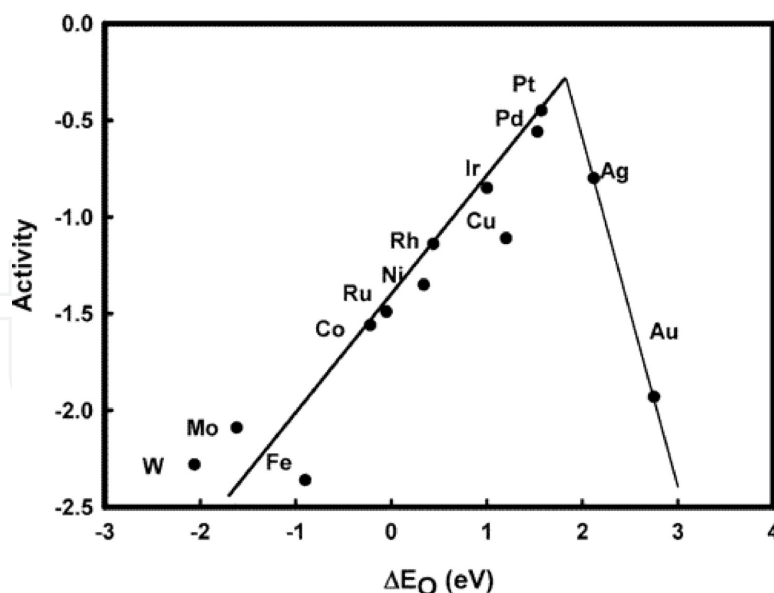


**Figure 1.** Variation of activity with oxygen adsorption energy for metals. Reproduced with permission from ref. 8. Copyright 2004, American Chemical Society.

superior activity as compared to the bulk alloys. This is accompanied with the reduction of cost of precious metal cost such as Pt in skin alloys by using a monolayer thick platinum on top of a non-precious metal/alloy core. As the skin is of Pt, therefore, stability in the corrosive chemical environment is still maintained in these alloys. The enhancement in the activity of these skin alloys is attributed to the geometric and ligand effect of the subsurface atoms on the skin. Recently, these structural form alloys have been reported to improve the ORR performance of the silver-based alloys. Some possible modifications of the surface electronic structure by the ligand mechanism are revealed in Figure 2.

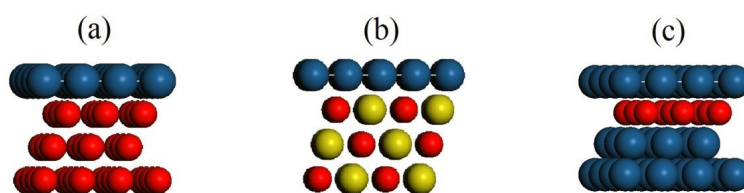


**Figure 2.** Modification of the surface geometric and electronic structure by subsurface configuration (a) skin on pure metal, (b) skin on alloy/compound, (c) subsurface ligand.

The rate-limiting step for ORR in case of Pt catalyst is the removal of adsorbed OH species. It is well established that the decrease in binding energy by 0.1–0.2 eV will optimize the performance of the Pt-based catalyst [13,14]. By using the Pt skin on a transition metal core, this reduction in binding energy can be achieved. This is attributed to the modification of the electronic structure of the surface atoms by the core. In case of transition metals such as Ti, Co, Ni, and Ru, charge transfers from the core to the d-band of the surface atoms of platinum [15]. This occupancy of d-band lowers the d-band centre of the platinum atoms which in turns

decreases the adsorption of the OH on the Pt skin. As a result of this mechanism, the activity of these alloy systems has been reported to be much superior than that of commercial Pt/C catalyst. The skin of platinum atoms can be either in compression or tension. This is because of the subsurface structure effect on the skin alloy. The compression of the Pt skin increases the overlap of the d orbitals which consequently increases the dband width. The result of this perturbation of the structure is the lowering of the dband center of the surface atoms [16, 17]. According to the dband theory, the lower the dband center of the surface, the lower its reactivity and vice versa. By the combination of geometric and ligand effects, the dband center of the surface can be tuned to the desired value so as to achieve the optimum adsorption of adsorbates such as O, OH and OOH on the surface of the metal. This is in accordance with the Sabatier principle which implies that for the catalytically induced chemical reactions catalyst for the reaction should have neither strong nor weak adsorption for the reaction species [18].

From Figure 1, it is evident that weak binding of oxygen onto silver is the cause of its shift from the volcano peak and weak ORR activity.

The oxygen reduction reaction for alkaline can occur by a direct four electron transfer method as in Eq. 2 or by indirect 2e transfers [19–21] as:



In the indirect mechanism, second step, i.e., Eq. (4), is the rate-determining step. The oxygen reduction reaction by indirect mechanism seriously limits the performance of the cell. This is because of the fact that if the reaction 4 does not occur by direct mechanism, then the total electrons transferred during ORR reduce to two only. As the result, this lowers the total output voltage and energy density. Also the peroxide formed in Eq. (3) can undergo catalyst-induced conversion to  $O_2$  and  $OH^-$  by Eq. (5).



Reaction 5 limits the catalytic activity of the catalyst and hence it is desirable that the ORR proceeds by direct four electron transfer mechanism. The effect of pH on the ORR mechanism has been studied by Blizanac et al. [22]. In case of ORR on Ag(111) in alkaline medium, four electron transfer was found to be the dominant mechanism at all overpotentials, but in case of low pH, i.e., in acidic solutions, 2 electron pathway was favored at low overpotentials. It was observed that the ORR on Ag (111) by 4 electron pathway could take place only at high overpotentials in the low pH electrolytes.

Owing to the stability and efficient ORR mechanism of silver-based catalysts in alkaline media, various research groups have focused on the synthesis of Ag-based catalysts. Holewinski et

al. have investigated the effect of alloying on silver for the ORR performance [23]. Density functional theory (DFT) based calculations were performed on Ag alloy slabs with an Ag skin on top to investigate the effect of alloy core on the ORR performance. The 4 electrons transfer has been proposed by the following mechanism:



A reaction coordinate diagram was developed for different alloys of silver on the basis of DFT calculation for the above mentioned reactions. From the theoretical calculations it was concluded that in case of silver-based catalysts, the rate-determining step for ORR is the initial adsorption of oxygen on the catalyst surface to form OOH adsorbate. In order to confirm the theoretical findings, the group synthesized Ag-Co alloys. After chemical etching of the alloy an Ag-skin with an Ag-Co core was developed. The resulting silver alloy showed phenomenal improvement in the ORR as compared to the unalloyed catalyst. Functionality tests on the Ag-skin /Ag-Co alloy core yielded an improvement in the area specific activity by a factor of 6 @ 0.8 V<sub>RHE</sub>. This significant enhancement was attributed to the perturbation of the electronic structure of the surface silver atoms which resulted in the lowering of the activation energy barriers for the ORR.

Composites of silver/graphene oxide and silver/graphene oxide/carbon were developed to investigate their ORR performance in alkaline environment [24]. The composites were facially synthesized by the reduction of AgNO<sub>3</sub> with graphene oxide with or without the presence of Vulcan XC-72 carbon black. The average particle size of Ag/CO/C composites (ca d = 12.9 nm) was found to be almost twice of Ag/CO composite (ca d = 6.9). The composites were electrochemically characterized which revealed the superior performance of Ag/CO/C for ORR as compared to Ag/CO composite. Rotating disc electrode (RDE) analysis revealed that the onset potential and the half wave potential shift positively for Ag/CO/C as compared to Ag/CO composite. This enhancement in ORR performance of Ag/CO/C composites as compared to Ag/CO composites was attributed to the 3D composite support which not only improves the electrical conductivity but also facilitated the mass transport in the catalyst layer. A similar beneficial effect of catalyst support was observed in the case of Ag/Mn<sub>3</sub>O<sub>4</sub>/C catalysts [25]. The catalyst performance for ORR in alkaline media was found to be superior to the simple Ag/C catalyst. This improvement was ascribed to the Mn<sub>3</sub>O<sub>4</sub> support which perturbed the electronic



structure of the silver particles. Charge was transferred to  $\text{Mn}_3\text{O}_4$  support from Ag which was manifested by the lowering of the binding energy of the Ag 3d electrons in XPS measurements. This was accompanied with the rise of the d-band center of Ag in the Ag/ $\text{Mn}_3\text{O}_4$ /C catalyst as compared to the Ag/C catalyst. This was attributed to the tensile strain which results in less overlap of d orbitals and a corresponding rise of the d-band center which in turn favors the kinetics of ORR by O—O bond breakage. Figure 3 reveals the oxygen reduction polarization curves for Ag/C, Ag/ $\text{Mn}_3\text{O}_4$ /C and Pt/C at 1600 rpm in  $\text{O}_2$ -saturated 0.1 M KOH. The onset potential for Ag/ $\text{Mn}_3\text{O}_4$ /C was 0.92 V (vs. RHE) which is close to the onset potential for Pt/C catalyst. The limiting current incase of Ag/ $\text{Mn}_3\text{O}_4$ /C (c.a.  $I_l = 5.5 \text{ mA/cm}^2$ ) was also found to be very close to the limiting current of Pt/C (c.a.  $I_l = 5.62 \text{ mA/cm}^2$ ). Moreover, the electron transfer mechanism was found to proceed by four electrons from the Koutecky–Levich plots.

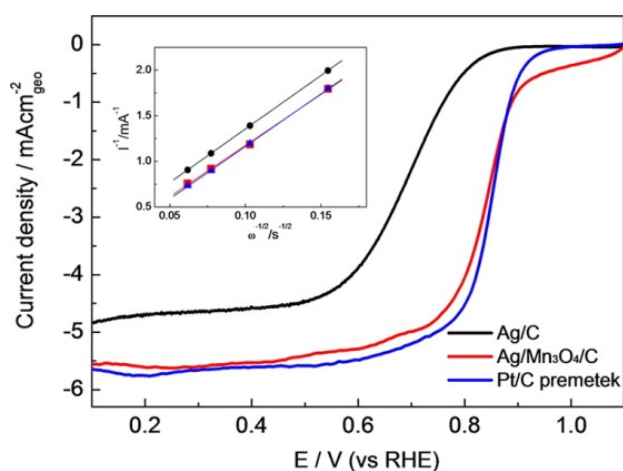


**Figure 3.** Oxygen reduction polarization curves for Ag/C, Ag/ $\text{Mn}_3\text{O}_4$ /C and Pt/C premetek at 1,600 rpm in  $\text{O}_2$ -saturated 0.1 M KOH at  $10 \text{ mV s}^{-1}$ , and (inset) Koutecky–Levich plots for ORR in the presence of Ag/C, Ag/ $\text{Mn}_3\text{O}_4$ /C and Pt/C premetek at 0.32 V vs. RHE. Reproduced with permission from ref. 25. Copyright 2015, American Chemical Society.

The effect of morphology of the silver catalyst particles was studied by Ohyama et al. [26]. Silver particles with three distinct morphologies were investigated for their ORR performance in alkaline medium. Among the spherical, worm-like and the faceted particles, the maximum specific activity was observed in the worm-like particles with subsurface oxygen at surface defects. This was followed by the multifaceted particles with surface  $\text{AgCO}_3$  layer and defects. The smooth and spherical particles had the least specific activity of the three types. This increase in activity is justified by the large number of defects on these irregular-shaped particles which increase the reactivity of the silver catalyst toward the  $\text{O}_2$  during ORR.

## 2. Computational work

The computational work involves initially the search for the structure with global minimum energy by genetic algorithm. The structure with minimum energy is further optimized by

density functional theory (DFT) calculations. The most optimum structures are employed for simulations of the ORR reactions by density functional theory calculations.

## 2.1. Structural optimization

The first step toward computational modeling of the nanoalloys is to search for the most stable geometry at absolute zero. This requires the modeling of the potential energy surface for the multi-element alloy. Gupta potential was used for the atomistic modeling of the nanoalloy [27, 28]. It is a semi-empirical method for the approximation of the potential energy surface. This method is based on the second moment approximation to the tight binding theory (SMATB). Total energy  $E$  for the nanoalloy  $A_xB_{N-x}$  is written as a sum of an attractive term  $E_j^b$  and a repulsive term  $E_j^r$ .

$$E = \sum_j (E_j^b + E_j^r) \quad (10)$$

where  $E_j^b$  and  $E_j^r$  are further defined as:

$$E_j^b = \sqrt{\sum_{i \neq j}^N \xi^2 e^{-2q(r_{ij}/r_0 - 1)}} \quad (11)$$

and

$$E_j^r = \sum_{i \neq j}^N A e^{-p \left( \frac{r_{ij}}{r_0} - 1 \right)} \quad (12)$$

$N$  is the number of atoms,  $r_{ij}$  is the distance between atoms  $i$  and  $j$  in the cluster and  $r_0$  is the nearest-neighbor distance. The parameters  $A$ ,  $r_0$ ,  $\xi$ ,  $p$  and  $q$  for the pure species are fitted to several bulk experimental values, such as the cohesive energy, the lattice parameter and the elastic constants. The heteroatom interactions are fitted to the solubility energy of an impurity  $A$  into a  $B$  bulk. The Gupta potential parameters used for the Ag–Cu system are listed in Table 1 [29].

Parameters	$A$ (eV)	$\xi$ (eV)	$p$	$q$	$r_0$ (Å)
Ag–Ag	0.1031	1.1895	10.85	3.18	2.8291
Ag–Cu	0.0980	1.2274	10.70	2.805	2.72405
Cu–Cu	0.0894	1.2799	10.55	2.43	2.556

**Table 1.** Gupta potential parameters for Ag–Cu system



From the modeling of the potential energy surface the next step forward is to search for the global minimum (GM) by optimization. This is performed by the help of Birmingham cluster genetic algorithm (GA) [30]. From the initially randomly generated cluster population, the algorithm looks for the most stable cluster structure by mutation and cross over. For each generation, parent clusters are chosen with a probability depending on their fitness and offsprings are developed from parents by a cross-over scheme which is followed by a mutation step on the offspring to bring diversity in population. The whole population is ranked by fitness and the less fit, i.e. high-energy, clusters are replaced with more stable structures. The whole process is repeated till a predefined convergence criterion is met.

The 13 atom Ag–Cu bimetallic cluster was chosen for further geometric optimization by Dmol<sup>3</sup> module available in the materials studio software package [31,32]. The 13 atom cluster is a magic size owing to special stability and relative abundance in case of Ag–Cu alloy clusters [33,34]. Spin-polarized DFT calculations are performed in real space within the framework of DFT-based semi core pseudo potentials (DSPPs) with the double numerical plus polarization (DNP) function. Grid integration is performed with a global cutoff of 5.0 °Å. Self-consistent field procedures are performed with a convergence criterion of 10<sup>-6</sup> Hartree on the total energy and the electron density. The Perdew et al. generalized gradient approximation (PBE/GGA) is used for the exchange–correlation functional during the geometry optimization for the Ag cluster. The ascending order of stability for the pure 13 atom Ag cluster is icosahedron (Ih) with binding energy  $E_b = -18.682$  eV, decahedron (Dh) with  $E_b = -18.731$  eV and cuboctahedron (COh) with  $E_b = -18.958$  eV, where cuboctahedron (COh) structure was found to be the most stable configuration for the 13 atom Ag cluster. In case of the single Cu surface-doped Ag<sub>12</sub>Cu cluster, the increasing order of stability is also icosahedron (Ih) with  $E_b = -19.18727$  eV, decahedron (Dh) with  $E_b = -19.40207$  eV and cuboctahedron (COh) with  $E_b = -19.55135$  eV. So for both pure Ag<sub>13</sub> and Ag<sub>12</sub>Cu<sub>surface</sub> clusters, the most stable structural form was found to be cuboctahedron (COh).

## 2.2. ORR on 13 atom Ag–Cu clusters

Ma et al. performed first principle calculations for the ORR process in alkaline media on the 13 atom pure Ag and Cu doped Ag clusters [35]. 13 atom Ag–Cu nanoalloy clusters have been previously identified as a potential candidate for ORR catalyst [36]. Pure Ag<sub>13</sub> and Ag<sub>12</sub>Cu<sub>surface</sub> clusters with cuboctahedron (COh) symmetry were used for these calculations. The doping of copper significantly improves the ORR process. The ORR reaction was observed to occur by the efficient four electron transfer mechanism. Pure silver is a poor catalyst for the ORR because of its weak adsorption of oxygen. Doping of silver with copper atom on the surface improves the binding of the intermediates such as O, OH and OOH on the nanoalloy cluster. This optimum binding is critical for the efficient ORR. Binding energies of different adsorbates are described in Table 2.

From Table 2 it is evident that the binding energy of every adsorbate is more negative on the Ag<sub>12</sub>Cu<sub>surface</sub> cluster as compared to pure Ag<sub>13</sub> cluster. This stronger binding facilitates the electron transfer reactions in the ORR process. A schematic of the ORR mechanism is provided in Figure 4.

ORR pathway	$\cdot\text{O}_2$	$\cdot\text{O}_2^-$	$\cdot\text{OOH}$	$\cdot\text{OOH}^-$	$\cdot\text{OH} + \cdot\text{OH}$	$\cdot\text{OH}$
$\text{Ag}_{13}$ (eV)	-0.216	-0.259	-1.144	-0.980	-4.594	-2.958
$\text{Ag}_{12}\text{Cu}$ (eV)	-1.019	-1.154	-1.697	-1.304	-5.405	-3.312

Table 2. Binding energy of different adsorbates on nanoclusters

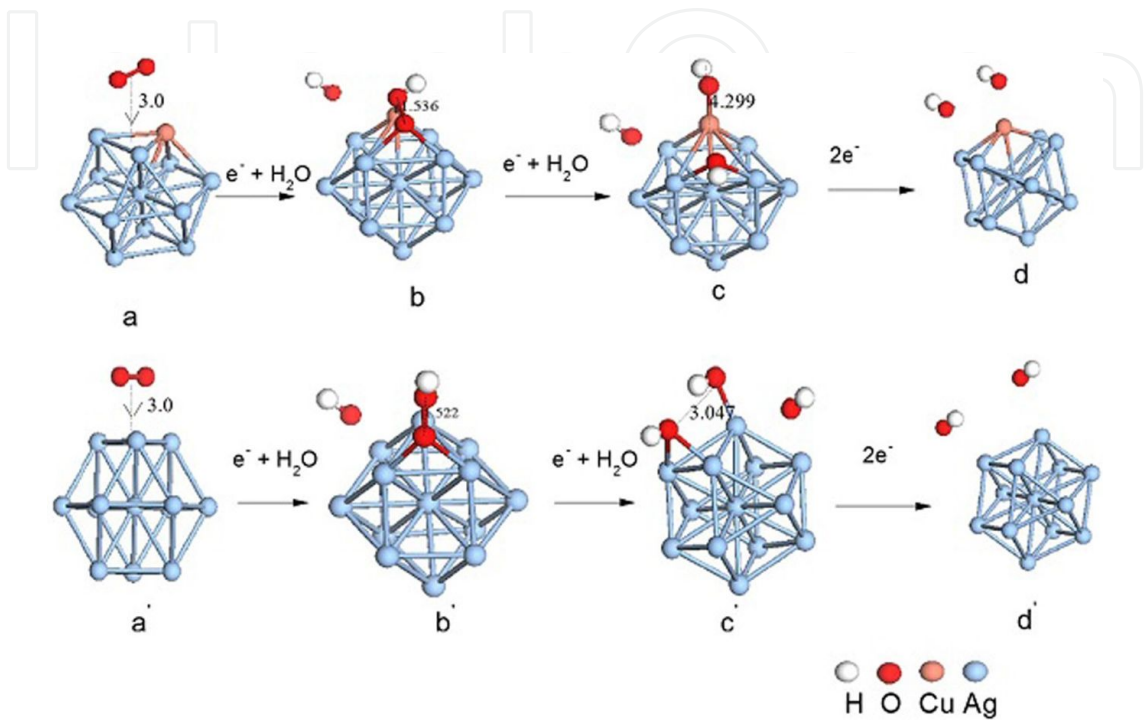


Figure 4. ORR pathway on  $\text{Ag}_{13}$ (a,b,c,d) and  $\text{Ag}_{12}\text{Cu}$  (a', b', c',d'). Reprinted with permission from ref. 35. Copyright 2014, Springer.

The improvement of the ORR performance of the copper doped 13 atom nanocluster can be attributed to the modification of the dband. The dband center of the  $\text{Ag}_{13}$  cluster is at  $-3.078$  eV. Doping with a copper atom at surface raises the dband center to  $-1.507$ eV. This can be explained by the dband theory of the reactivity of metal surfaces. According to that theory, the deeper the dband from the Fermi level, the lower is the surface reactivity. Alloying with copper raises the dband of the nanoalloy as compared to the pure metal cluster, which in turn raises the binding ability of the intermediates onto the nanoalloy cluster. The stronger binding of the intermediates is the reason behind the better ORR performance of  $\text{Ag}_{12}\text{Cu}$  cluster as compared to the  $\text{Ag}_{13}$  cluster.

2.3. ORR on 38 atom Ag–Cu clusters

The 38 atom  $\text{Ag}_{38-x}\text{Cu}_x$  cluster has been studied for ORR because of its relative stability by another group [37]. Truncated octahedron (TO)  $\text{Ag}_{32}\text{Cu}_6$  alloy cluster was observed to perform as a better catalyst for ORR as compared to the TO  $\text{Ag}_{32}\text{Cu}_6$  core-shell clusters. With the use of Gupta potential-based potential energy surface and genetic algorithm (GA) search for global minimum, polyicosahedron (PIh)  $\text{Ag}_{32}\text{Cu}_6$  core-shell structure is found to be the most stable

structure for  $\text{Ag}_{32}\text{Cu}_6$  nanoalloy by Zhang et al.[38]. The stability of polyicosahedron (PIh)  $\text{Ag}_{32}\text{Cu}_6$  core-shell structure exceeds that of truncated octahedron (TO)  $\text{Ag}_{32}\text{Cu}_6$  core shell by 0.564 eV. For both pure  $\text{Ag}_{38}$  and  $\text{Cu}_{38}$  clusters truncated octahedron (TO) was the most stable geometry. Figure 5 shows that the minimum energy structure of the pure 38 atom silver took 35 iterations while more than 70 iterations were required for the  $\text{Ag}_{32}\text{Cu}_6$  nanoalloy cluster.

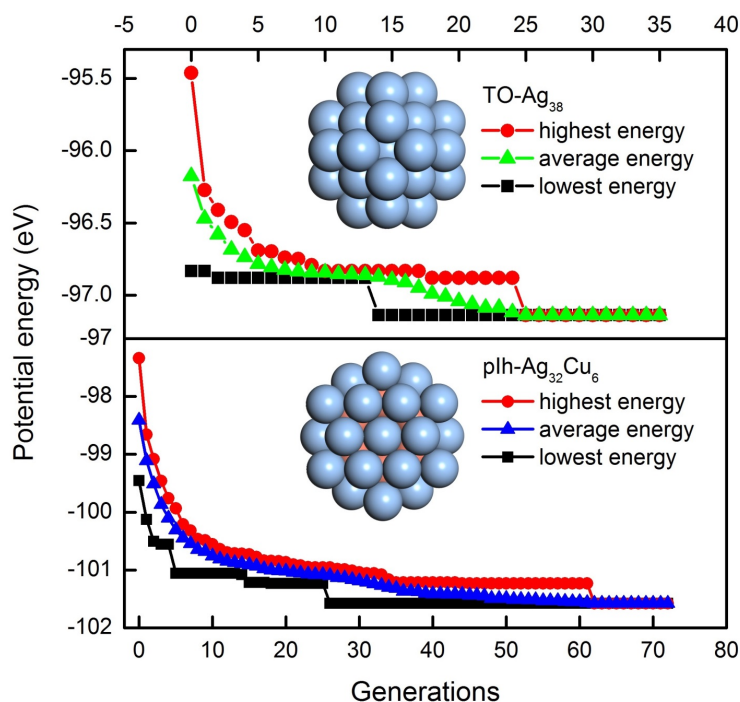


**Figure 5.** Generations to reach global minimum by genetic algorithm. Adapted from ref. 38.

The polyicosahedron (PIh)  $\text{Ag}_{32}\text{Cu}_6$  core-shell structure was further investigated for ORR because of its stability. ORR was found to proceed more favorably by the dissociation mechanism as compared to the associative mechanism by 0.1 eV. Hence, dissociative ORR mechanism involving the scission of molecular oxygen to atomic form, i.e.,  $\text{O}_2 \rightarrow \text{O} + \text{O}$ , was considered for computational analysis. Four non-equivalent sites were identified on the  $\text{Ag}_{32}\text{Cu}_6$  core-shell structure as B1 to B4. The ORR was then followed with the bond fracture and subsequent adsorption of atomic oxygen at hollow sites marked H1, H2 and H3 as shown in Figure 6.

Of the four adsorption configurations, we notice that the adsorption energy on B4 site has a highest value of -0.149 eV, and also the maximum value of 1.209 eV for the dissociation barrier, and an energy release of 0.259 eV, dissociating to H2 and H3 sites. The B1 site, which has similar adsorption energy to B4 site, -0.146 eV, further dissociates to two H2 sites with barrier of 0.993 eV and exothermicity of 0.259 eV. The  $\text{O}_2$  on B2 and B3 sites have bond-cleavage barriers of 0.715 and 1.134 eV and energy release of 1.088 and 0.368 eV, respectively. It is clear that the most favorable pathway for  $\text{O}_2$  dissociation is B2 sites with a minimum value of activation energy barrier.

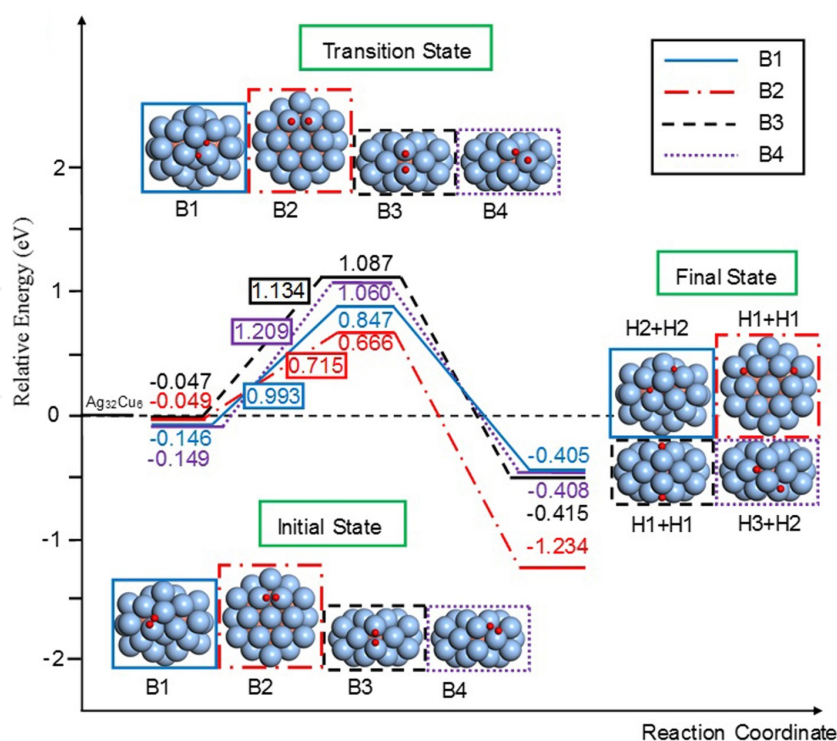


**Figure 6.** Reaction coordinate diagram. Adapted from ref. 38.

The interaction strength of atoms and molecules with metal surface is defined by the *d*-band center of the metal. In order to explain further that B2 site is most favorable to display a good catalytic behavior, the electronic structure of these four adsorption configurations was addressed and the position of the *d*-band center relative to the Fermi energy for these different sites was calculated as shown in Figure 7. The *d*band center of B2 site is  $-3.395$  eV, which is closest to the Fermi level. By having the *d*band center closest to the Fermi level as compared to the other adsorption sites on the polyicosahedron (PIh)  $\text{Ag}_{32}\text{Cu}_6$  core-shell structure, B2 site is the most conducive for ORR as it enhances the otherwise weak affinity of silver alloys for the reaction intermediates.

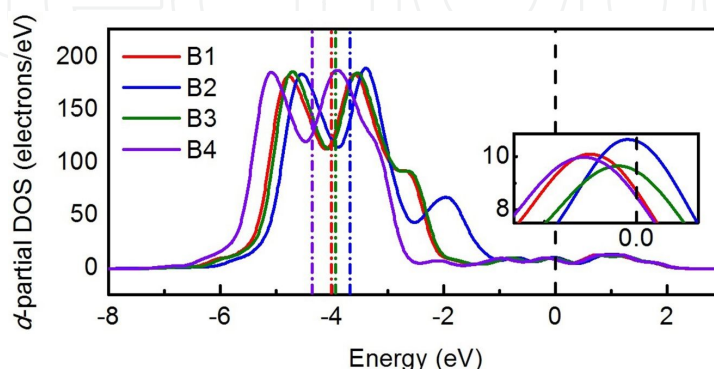


**Figure 7.** Partial density of states (PDOS). Adapted from ref. 38.



Moreover, frontier orbital theory describes that the states of a metal which are involved in electron transfer with the adsorbates are closest to the Fermi level [39]. Therefore, the density of states (DOS) at the Fermi level is an indicator of the chemical activity. We notice that the density of states at the Fermi energy level is maximal for B2 site. This further endorses the superior activity of the B2 site for ORR on  $\text{Ag}_{32}\text{Cu}_6$  core-shell nanoalloy.

### 3. Synthesis of Ag–Cu nanoalloy

Bimetallic Ag–Cu nanoalloy particles were developed by both physical and chemical routes.

#### 3.1. Pulse laser deposition

Pulse laser deposition (PLD) is widely used in the field because the approach is a feasible way to control the thickness of catalyst layer [40]. As the utilization of catalyst in the fuel cell is determined mainly by the surface area of catalyst with electrolyte, the reduction of the thickness of catalytic layer can lead to improvement of the catalyst utilization and reduction of the fuel cell cost [41]. Moreover, compared to chemical preparation techniques such as electrochemical deposition, chemical vapor deposition, reduction of salts and facile hydrothermal method, PLD method owns high repeatability and stability in process, making it to be a suitable route to obtain electrocatalyst with film state [42–44].

Ag–Cu alloyed catalyst was developed by PLD method in a vacuum chamber [45]. The target of Ag–Cu alloy with atomic ratio of 50:50 was irradiated with a nanosecond Q-switched Nd:YAG laser beam (EKSPLA, Lithuania). The wavelength was set to be 266 nm, and the pulse duration was ranging from 3 to 6 ns. The laser beam diameter was around 1 mm, with an energy density of 200 mJ/pulse. Both target and substrate (nickel foam) rotated at a speed of 5 rpm during deposition, and target was irradiated for 2 min at 10 Hz to clear away the oxide on the surface before deposition. The laser was operated at the frequency of 10 Hz. The deposition time is set as 90 min. The as-prepared product is  $\text{Ag}_{50}\text{Cu}_{50}$  catalyst.

Figure 8 shows series of TEM analysis on  $\text{Ag}_{50}\text{Cu}_{50}$  catalyst. According to Figure 8a, plenty of nanoparticles are distributed in a continuous film. The tiny nanoparticles with size under 5 nm dominate the film. Magnifying the blue rectangle area, the obtained HRTEM is shown in Figure 8b. It can be seen that they display two different states: few are amorphous, and the left are with crystallized state.

HAADF result shown in Figure 8c displays that contrast of the particles is brighter than the gap area between particles, demonstrating a higher atomic number  $Z$  for nanoparticles. The lower  $Z$  corresponding gap area then is attributed from Cu element. This is because  $Z$  of Cu ( $Z = 29$ ) is smaller than Ag ( $Z = 47$ ). Combining the amorphous state in gap area observed in Figure 8b, we can draw that  $\text{Ag}_{50}\text{Cu}_{50}$  catalyst actually is Ag–Cu alloyed nanoparticles embedded in amorphous Cu film.

Electrochemical characterizations have been carried out on PLD synthesized  $\text{Ag}_{50}\text{Cu}_{50}$  catalyst. Figure 9a shows RDE polarization curves of  $\text{Ag}_{50}\text{Cu}_{50}$  catalyst with rotation rate 1,600 rpm in

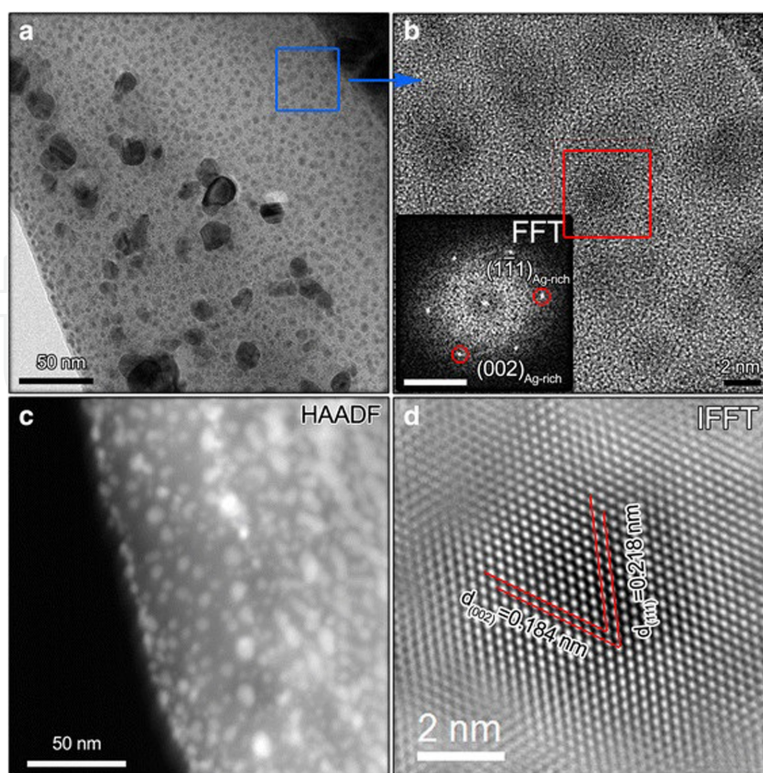


**Figure 8.** TEM and HAADF characterization of Ag<sub>50</sub>Cu<sub>50</sub> catalysts. (a) bright field image, (b) HRTEM, (c) HAADF result and (d) IFFT image. Adapted from ref. 45.

N<sub>2</sub> and O<sub>2</sub> saturated 0.1 M KOH solutions. It can be seen that there is reduction in current density in O<sub>2</sub>-saturated KOH solution, while that in N<sub>2</sub>-saturated solution is flat. This shows that the catalyst indeed works on O<sub>2</sub>. Figure 9b shows a set of RDE curves with rotation rates of 400, 800, 1,200 and 1,600 rpm. The Koutecky–Levich plots were then obtained from the limiting current density, as shown in Figure 9c. The plots show the inverse current density  $J^{-1}$  as a function of  $\omega^{-1/2}$ . From these plots the number of electrons transferred during ORR was found to be 3.76, 3.87, 3.85 and 3.97 when the potential was 0.5, 0.4, 0.3 and 0.2 V, respectively. Hence, four electrons route was found to be dominant for ORR in case of synthesized Ag<sub>50</sub>Cu<sub>50</sub> catalyst. Finally, 9d gives a comparison of the performance of Ag, Ag<sub>50</sub>Cu<sub>50</sub> and Pt/C(20 wt%).

The catalytic layer was used to assemble a zinc-air battery and results showed open-circuit voltage (OCV) of the cell was around 1.48 V close to the theoretical value, and the maximum power density is 67 mW cm<sup>-2</sup> at 100 mA cm<sup>-2</sup>. The resulting rechargeable zinc-air battery exhibits low charge–discharge voltage polarization of 1.1 V at 20 mAcm<sup>-2</sup> and high durability over 100 cycles in natural air.

Wu et al. deposited Ag–Cu nanoalloys on nickel foam by pulse laser deposition. Several Ag–Cu alloys with Ag/Cu atom ratios of 90:10, 50:50 and 25:75 are used as the target material with the high-purity nickel foam (99.97%) as substrate [46]. Ag–Cu nanoalloys were used as the catalyst layer of the air cathode for a single zinc-air battery, and found to exhibit good



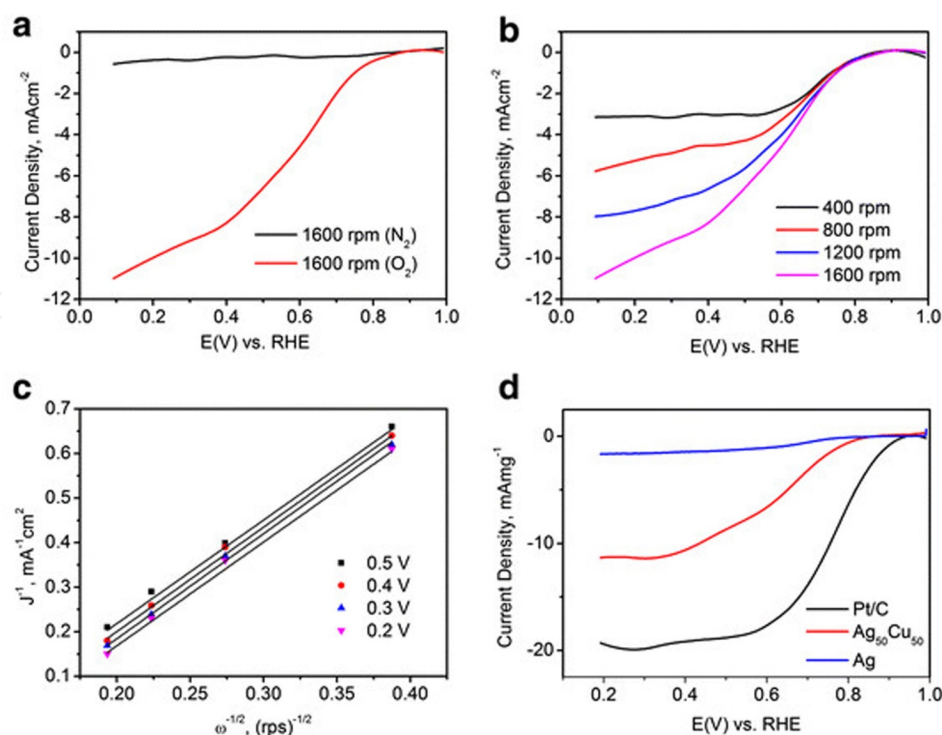


**Figure 9.** Electrochemical characterization of  $\text{Ag}_{50}\text{Cu}_{50}$  catalyst. (a) The RDE curves of  $\text{Ag}_{50}\text{Cu}_{50}$  catalyst in  $\text{O}_2$ - and  $\text{N}_2$ -saturated 0.1 M KOH solution; (b) the RDE curves at the rotation rates of 400, 800, 1,200 and 1,600 rpm; (c) the Koutecky-Levich plot of  $\text{Ag}_{50}\text{Cu}_{50}$  catalyst; and (d) the ORR mass activity for Ag,  $\text{Ag}_{50}\text{Cu}_{50}$  and Pt/C (20 wt%) catalysts. Adapted from ref. 45.

bifunctional catalytic performance. The effect of the Ag/Cu atom ratio on the average electron transfer numbers of the ORR was systematically investigated. This carbon-free binder-free bimetallic catalyst layer was found to possess both ORR and OER catalytic activity in the rechargeable zinc-air battery. Figure 10(a) shows representative microscopic images of the  $\text{Ag}_{50}\text{Cu}_{50}$  alloys used in this work. The Ag–Cu nanoparticles were uniformly distributed in the substrate, and the electron diffraction pattern revealed the single phase and polycrystalline structure of the Ag–Cu alloy. Figure 10(b) shows a HRTEM image of more than 100 nanoparticles in the substrates. It is clear that the nanoparticles have an average size of 2.58 nm with a narrow size distribution between 1 and 5 nm. Figure 10(c,d) indicate that the nanoparticles are enriched with Ag atoms, with few doped copper atoms in them, and the films are enriched with Cu atoms.

Hence, it can be concluded that the nanocatalyst has crystalline Ag-enriched nanoparticles embedded in an amorphous Cu-enriched matrix. These copper-doped silver nanoparticles with composition  $\text{Ag}_{50}\text{Cu}_{50}$  were observed to have superior catalytic performance for ORR as compared to pure silver as shown in Figure 11. The ORR was found to proceed via four electron transfer mechanism. It is for the first time the Ag-based electrocatalysts in amorphous films were created from the vapor phase under far-from-equilibrium condition by pulse laser ablation, previous works demonstrated that the face-centered cubic Ag–Cu solid solutions or completely amorphous Ag–Cu metal glasses were formed by rapid quenching from the liquid or vapor phase as corrosion-resistant non-equilibrium alloys and metastable phases.

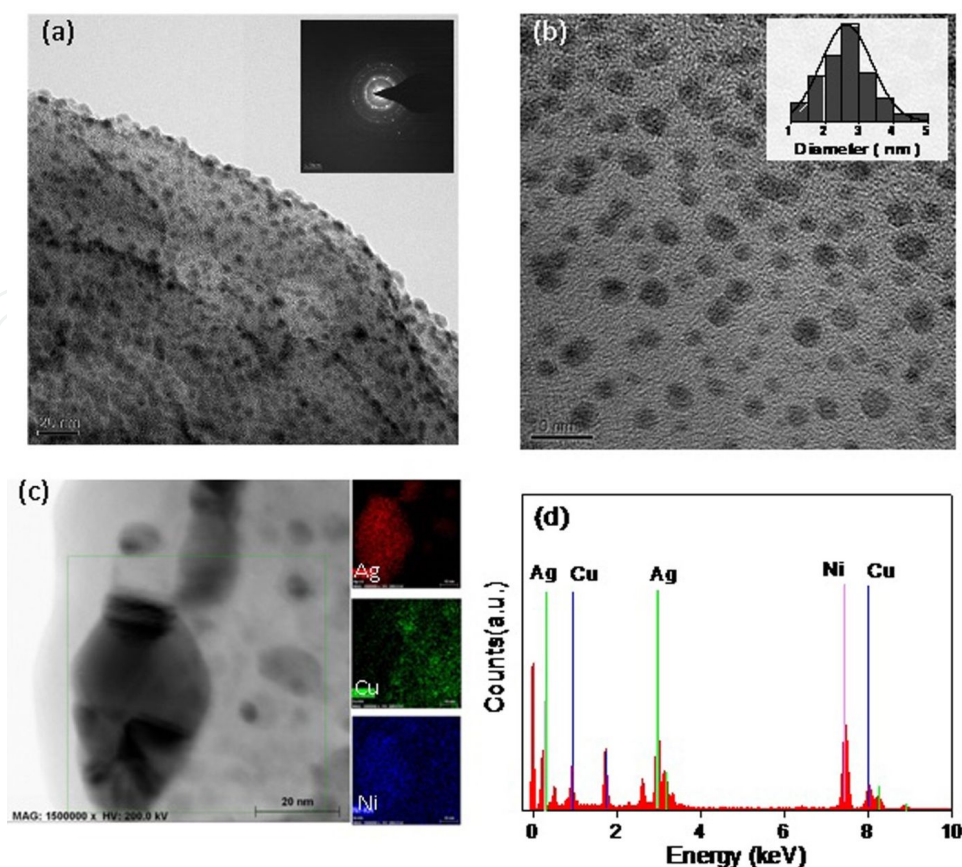


**Figure 10.** (a) TEM bright-field images and SAED patterns (inset) of the Ag<sub>50</sub>Cu<sub>50</sub> film prepared by PLD. (b) HRTEM images and the particle size distribution (inlet) of Ag-Cu nanoparticles in the film. (c) TEM element mapping for Ag, Cu and Ni on a Ag-Cu nanoparticle deposited on nickel grid. (d) EDS of the Ag<sub>50</sub>Cu<sub>50</sub> film on nickel grid. Reprinted with permission from ref. 46. Copyright 2015, American Chemical Society.

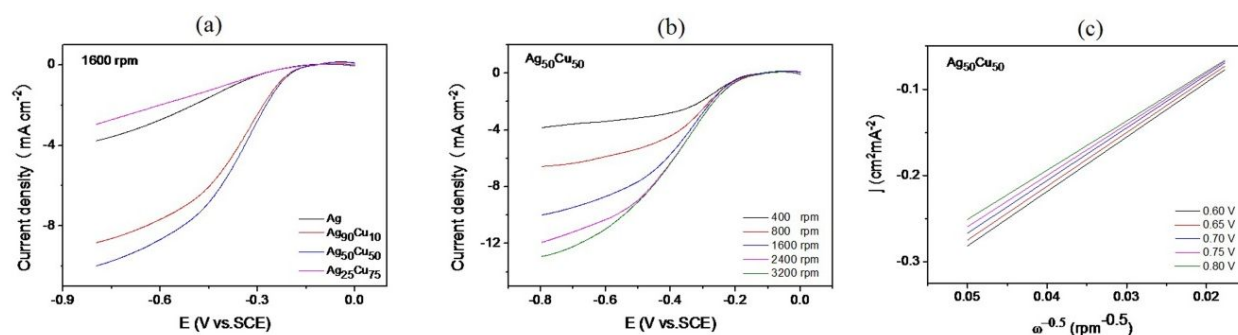


**Figure 11.** (a) RDE polarization curve of different compositions in O<sub>2</sub>-saturated 0.1 M KOH solution. (b) RDE polarization curve for Ag<sub>50</sub>Cu<sub>50</sub> same environment (c) Koutecky-Levich plots for (b). Reprinted with permission from ref. 46. Copyright 2015, American Chemical Society.

Zinc-air batteries were assembled using Ag<sub>90</sub>Cu<sub>10</sub> and Ag<sub>50</sub>Cu<sub>50</sub> catalysts in the air cathode, and the discharge performance is shown in Figure 12(a). The cell voltage decreases nearly with increasing current density, demonstrating that the cell performance shows a strong dependence on the resistance of the battery. For Ag<sub>50</sub>Cu<sub>50</sub> and Ag<sub>90</sub>Cu<sub>10</sub> catalysts, the open-circuit

voltages of the single cell are about 1.42 V and 1.44 V, the peak power densities of the zinc-air batteries are  $86.3 \text{ mW}\cdot\text{cm}^{-2}$  and  $82.1 \text{ mW}\cdot\text{cm}^{-2}$  and the current densities at a voltage of 1 V are  $60 \text{ mA cm}^{-2}$  and  $50 \text{ mA cm}^{-2}$ , which is higher than Ag/C, N-doped CNTs and silver-molybdate catalysts [47,48]. Figure 12 (b) records the change of cell voltage with time at a current density of  $20 \text{ mA cm}^{-2}$ . It is clear that  $\text{Ag}_{90}\text{Cu}_{10}$  catalysts have a higher initial discharge voltage of 1.15 V than  $\text{Ag}_{50}\text{Cu}_{50}$  catalysts (1.0V); however, after 30 h discharging, the discharge voltage of  $\text{Ag}_{90}\text{Cu}_{10}$  catalysts gradually reduces to 1.11 V, while  $\text{Ag}_{50}\text{Cu}_{50}$  catalysts gradually increase to 1.18 V. The discharge curve of the  $\text{Ag}_{50}\text{Cu}_{50}$  catalysts gradually rises to a stable cell voltage and decrease by 16% as compared with the open-circuit potential, but for  $\text{Ag}_{90}\text{Cu}_{10}$  catalysts, the curve gradually reduces to a stable voltage after about 30 h of discharge, showing a decrease of 20%. It can be concluded that the  $\text{Ag}_{50}\text{Cu}_{50}$  catalyst has higher discharge voltage stability, being more stable than the  $\text{Ag}_{90}\text{Cu}_{10}$  catalysts for applications in zinc-air batteries.

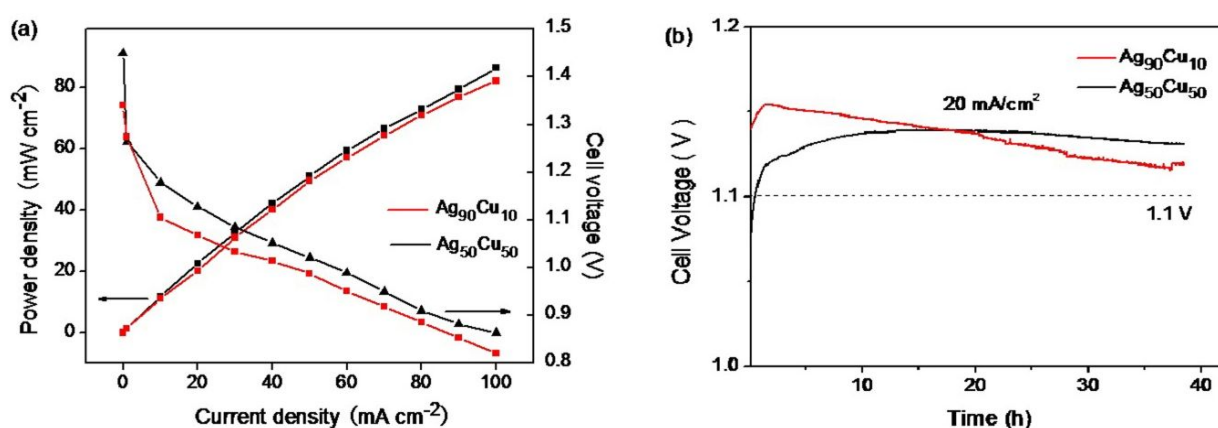


**Figure 12.** (a) The discharge polarization and power density curves for  $\text{Ag}_{90}\text{Cu}_{10}$  and  $\text{Ag}_{50}\text{Cu}_{50}$  catalyst layer of air-cathode in the primary zinc-air battery. (b) The single cell voltage and time curves at  $20 \text{ mA cm}^{-2}$  in the primary zinc-air battery. (In 6M KOH solution) Reprinted with permission from ref. 46. Copyright 2015, American Chemical Society.

### 3.2. Galvanic displacement synthesis

Ag–Cu catalysts were synthesized directly on Ni foams by galvanic displacement reaction, which is an environment-friendly and straightforward process [42]. In this method, the catalysts were directly grown on Ni foams, thereby freeing the catalytic layer from carbon and binder. The driving mechanism to grow the various catalysts in this work is the large difference of the redox potentials of  $\text{Ni}^{2+}/\text{Ni}$  ( $-0.25 \text{ V vs. SHE}$ ),  $\text{Cu}^{2+}/\text{Cu}$  ( $0.34 \text{ V vs. SHE}$ ) and  $\text{Ag}^{+}/\text{Ag}$  ( $0.799 \text{ V vs. SHE}$ ). The galvanic displacement reaction can be described by the following equations:

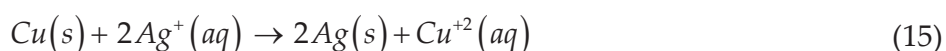
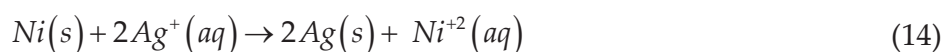
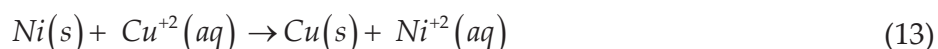
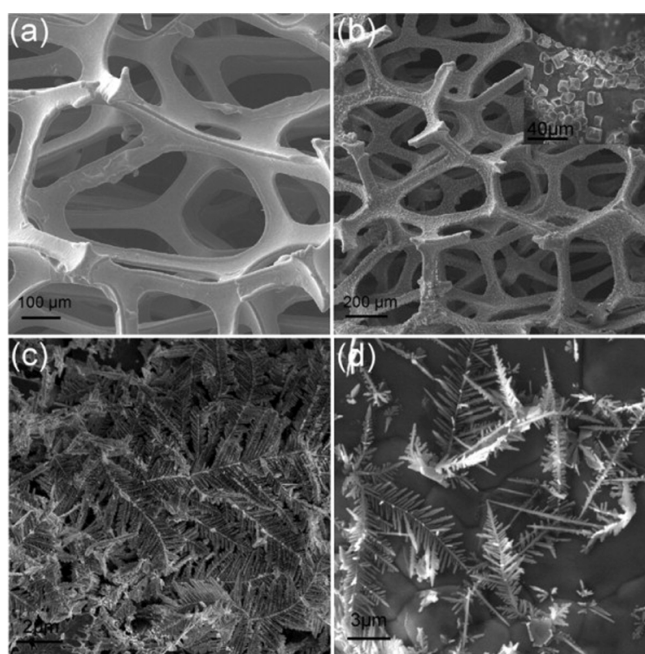


Figure 13 shows the typical SEM images of (a) Ni foam, (b) Cu nanoparticles, (c) AgCu-10 and (d) Ag catalysts. Figure 13(a) shows the pure Ni foam smooth surface. Immersion into  $\text{CuSO}_4$  solution for 3 h makes the surface of the foam rough (Figure 13(b)) along with coverage of octahedral copper nanoparticles (Figure 13(b) inset). The SEM of AgCu-10 catalyst prepared by two-step galvanic displacement reaction is shown in Figure 13(c). The catalyst has dendritic morphology. The dendrites shown in Figure 13(c) have a dense and uniform distribution, and the shape is complete. On the other hand, similarly dendritic morphologies are obtained for pure Ag catalyst (Figure 13(d)) prepared by directly immersing the as-prepared Ni foam into  $\text{AgNO}_3$  solution. The dendrites of Ag catalyst are thinly distributed on the Ni foam compared to that in Figure 13(c). The difference of the dendrites between AgCu-10 and Ag catalysts can be because of the different sacrificial templates. For the AgCu-10 catalyst, the Ni foam was already covered by octahedral copper nanoparticles while the nickel surface was free from copper in case of pure Ag particles.



**Figure 13.** The FE-SEM images of (a) Ni foam. (b) Cu nanoparticles supported on Ni foam. The inset in (b) shows the high-magnification image of Cu nanoparticles. (c) Ag-Cu dendrites in AgCu-10 catalyst and (d) Ag dendrites supported on Ni foam. Reprinted with permission from ref. 42. Copyright 2015, Elsevier.

As shown in Figure 13(c), the one-dimensional dendrites prefer to form in a relatively high  $\text{AgNO}_3$  concentration (10 mM). The AgCu-10 bimetallic catalyst possessed a hierarchical structure characteristic and highly rough surface which provided more catalytic active sites so it showed higher catalytic current during the RDE polarization measurements. The SEM elemental mapping analysis for AgCu-10 catalyst shown in Figure 14(a–d) clearly prove that Ag and Cu are uniformly distributed. HRTEM and SAED images are shown in Figure 14 (e, f). The clear lattice fringes are observed for AgCu-10 catalyst. The SAED pattern shows a typical polycrystalline structure with the sharp diffraction rings for AgCu-10 catalyst. The diffraction spots for Ag (111), (2 0 0), (2 2 0), (311) facets and Cu (111), (2 2 0) facets are observed. A fast



Fourier transform (FFT) diffraction pattern as shown in Figure 14 (g) is obtained on the area marked by the red rectangle in Figure 14 (e), exhibiting the two phases characteristic of AgCu-10 catalyst. The FFT image also reveals that Ag and Cu crystallites are in an epitaxial relationship relative to each other in parallel orientation. The grown orientation schematic is shown in Figure 14 (h).

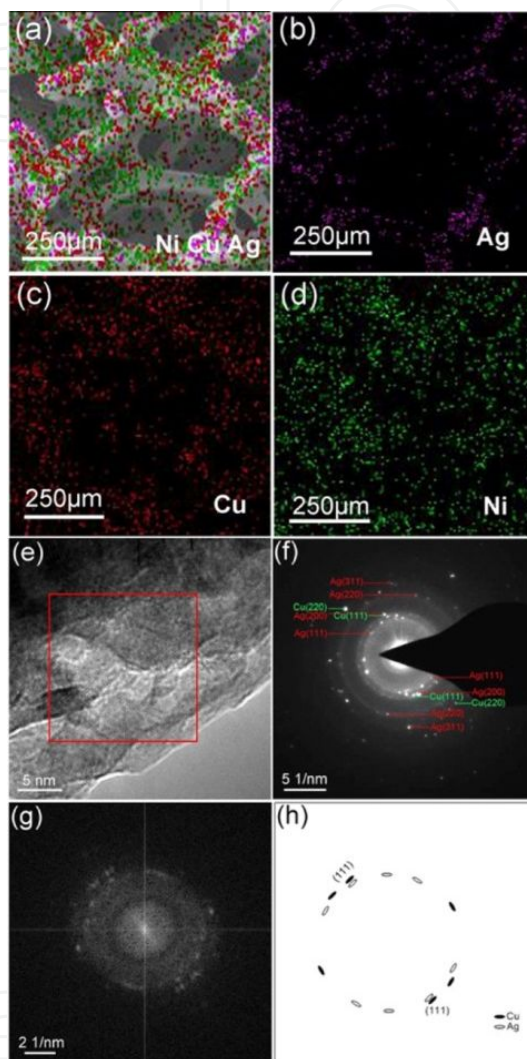


**Figure 14.** EDS elemental map of the AgCu-10 catalyst: (a) Overlay image. (b) Ag map. (c) Cu map. (d) Ni map. The TEM characteristic for AgCu-10 catalyst: (e) HRTEM image. (f) SAED pattern. (g) Fast Fourier transform (FFT) image corresponding to (e) and schematic drawing with index of reflections (h). Reprinted with permission from ref. 42. Copyright 2015, Elsevier.

Rotating disc measurements were performed on the catalysts made by galvanic displacement and comparison was made with pure silver. AgCu-10 performed efficiently as compared to the pure silver particles in terms of both onset potential and the limiting current. The Koutecky–Levich plots revealed the four electron transfer mechanism during ORR. Rechargeable zinc-air battery was also fabricated by as-prepared AgCu-10 catalyst-based air cathode, 6 M KOH solution with 0.2 M zinc acetate (zinc acetate was dissolved in KOH to form zincate to

ensure reversible Zn electrochemical reactions at the anode) and pure zinc plate anode. A charge–discharge cycle experiment was performed with a short cycle period of 20 min and a long cycle period of 4 h at 20 mA cm<sup>-2</sup>. At the short cycle period, the initial charge and discharge potentials of AgCu-10 based rechargeable zinc-air battery are 2.04 and 1.1 V, respectively. The round-trip efficiency corresponding to the first cycle is 53.9%. There is almost no apparent fluctuation for the charge and discharge potentials of the rechargeable zinc-air battery through all the cyclic process. The round-trip efficiency after 100 cycles is 53.08% compared to the initial 53.9% with a little decline of 0.82%. A further cycle performance study with a long cycle period of 4 h was carried out with the same rechargeable zinc-air battery after replacing the zinc anode and the electrolyte. The rechargeable zinc-air battery also shows high cycling stability at the long cycle period. The increase in charge and discharge potentials difference from the first to tenth cycle is as little as 0.06 V, which is comparable to the tri-electrode rechargeable zinc-air battery [49]. The cycling stability obtained on AgCu-10 catalyst based zinc-air battery is certainly appealing and significant for the large-scale application of metal-air batteries and fuel cells.

### 3.3. Electro-deposition of Ag–Cu nanoalloys

Ag–Cu catalysts were synthesized by the electrodeposition method under a potential of –0.4 V for a period of 50 s by using the conventional three-electrode cell system [50]. For synthesis, AgNO<sub>3</sub>, Cu(NO<sub>3</sub>)<sub>2</sub>·3H<sub>2</sub>O and 3 mM sodium citrate (Na<sub>3</sub>C<sub>6</sub>H<sub>5</sub>O<sub>7</sub>) are mixed by deionized water with the formula of Ag<sub>x</sub>Cu<sub>100-x</sub> (labelled as Ag<sub>25</sub>Cu<sub>75</sub>, Ag<sub>50</sub>Cu<sub>50</sub> and Ag<sub>75</sub>Cu<sub>25</sub> for  $x = 25, 50$  and 75 mM, respectively).

Figure 15(a) describes the TEM and SEM (the inset) images of the bimetallic Ag–Cu catalyst. The nanoplatelets have diameters of 40–50 nm. The HRTEM analysis in Figure 15(b) clearly shows lattice fringes, indicating good crystallinity. The lattice spacing obtained from the HRTEM image is 0.239 nm. The particle demonstrates a single crystal pattern in the SAED of Figure 15(c), indicating that Ag–Cu catalysts grow larger by the oriented attachment from small Ag–Cu nanoparticles. The cell constant of the single crystal is 0.3986 nm, which is between the standard cell parameter of FCC-Ag ( $a = 0.4086$  nm) and FCC-Cu ( $a = 0.3615$  nm), suggesting that the Cu atoms are partially alloyed with the Ag atoms.

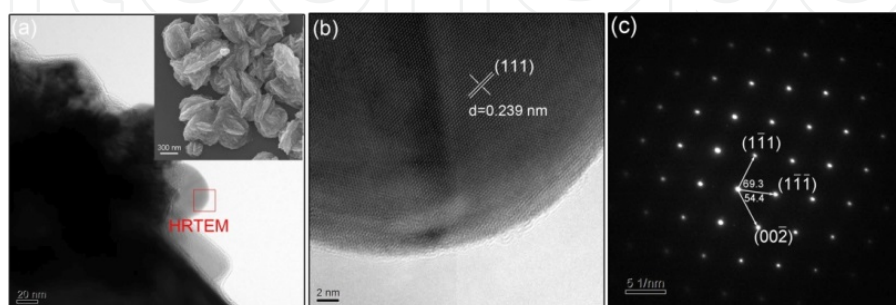


**Figure 15.** Images of the Ag–Cu catalyst (a) TEM (inset SEM). (b) HRTEM. (c) SAED. Reprinted with permission from ref. 50. Copyright 2015, John Wiley & Sons.



The EDX spectrum of the Ag–Cu nanoalloy in Figure 16(a) exhibits that the Ag–Cu deposits contain both Ag and Cu elements and the nominal atomic composition are 1.5:1, 5:1 and 10:1 for the Ag<sub>25</sub>Cu<sub>75</sub>, Ag<sub>50</sub>Cu<sub>50</sub> and Ag<sub>75</sub>Cu<sub>25</sub> samples, respectively.

The survey spectrum of XPS for the Ag–Cu catalyst is shown in Figure 16(b), which shows clear Ag and Cu peaks. The binding energies of the Ag3d<sub>3/2</sub> and Ag3d<sub>5/2</sub> orbits observed from the high-resolution spectrum (Figure 16(b) inset) are 374.4 and 368.4 eV. This result indicates that the Ag atoms are zero-valent (Ag<sup>0</sup>) metals [51,52]. The binding energies of the Cu2p<sub>1/2</sub> and Cu2p<sub>3/2</sub> orbits are 952.6 and 932.7 eV (Figure 16(f)). An analysis of the Auger electron spectrum for Cu LMM (Figure 16(f) inset) is also conducted to determine the specific valence of Cu; an apparent kinetic energy peak at 918.6 eV is seen, corresponding to the zero-valent Cu[53]. Thus, the Ag and Cu atoms exist as elemental metallic substances in Ag–Cu catalyst.

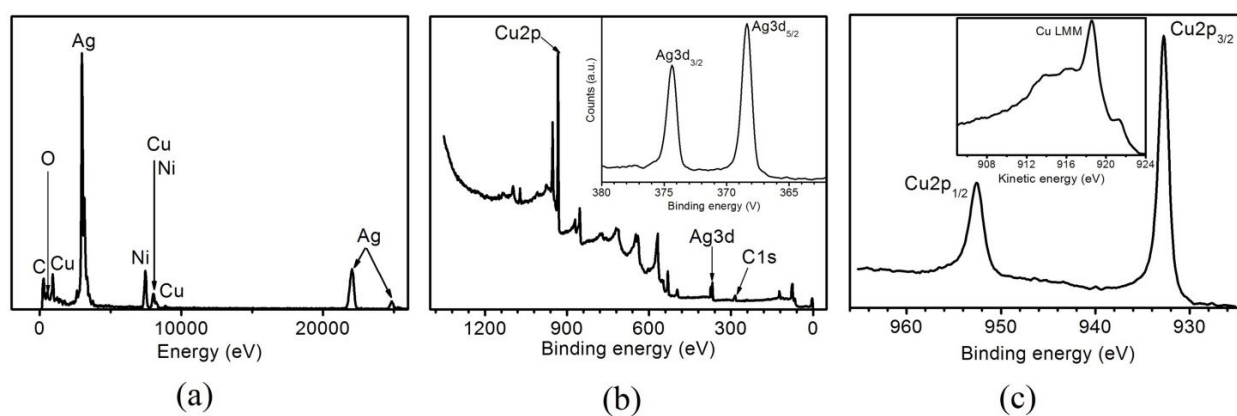


**Figure 16.** (a) EDX. (b) XPS survey spectrum, inset: high-resolution spectrum of Ag3d. (c) High-resolution spectrum of Cu2p, inset: Cu LMM. Reprinted with permission from ref. 50. Copyright 2015, John Wiley & Sons.

As shown in Figure 17(a), a reduction current peak is observed from the CV curves of the Ag–Cu catalyst in O<sub>2</sub>-saturated 0.1 M KOH at –0.3 V (vs. SCE) but not in N<sub>2</sub>-saturated solution, indicating that Ag–Cu catalyst has catalytic activity for ORR. To study the catalysis kinetics of Ag–Cu catalyst for ORR, an RDE experiment is performed in O<sub>2</sub>-saturated 0.1 M KOH solution (Figure 17(b)). The number (*n*) of electrons transferred on the Ag–Cu catalyst during ORR, which determines the catalytic efficiency, is calculated by the Koutecky–Levich plots (see inset). The result with *n* = 3.8 and 3.7 at –0.7 and –0.8 V, respectively, indicates that the ORR catalyzed by the Ag–Cu catalyst occurs through a four-electron pathway, which is more efficient than a two-electron pathway.

The performance of primary battery fabricated from Ag<sub>50</sub>Cu<sub>50</sub>-based air cathode was evaluated as shown in Figure 18(a). The open-circuit voltage (OCV) and maximum power density are 1.49 V and 87 mWcm<sup>–2</sup>, respectively, which have significant improvements [54,55]. After the primary zinc–air battery undergoes 10 discharging cycles, the OCV and power density decrease slightly. This result may be attributed to the polarization of the zinc anode caused by the zincate produced during the discharge process. Replacing the zinc anode and electrolyte revitalizes the battery performance. The battery has no obvious voltage loss compared with the first cycle, suggesting that the Ag<sub>50</sub>Cu<sub>50</sub>-based air cathode is stable in alkaline solution and

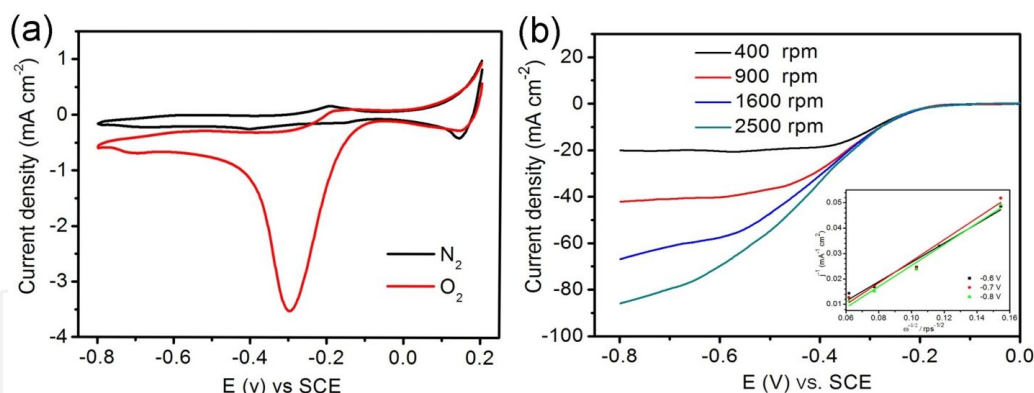


**Figure 17.** (a) CV curves for Ag-Cu catalyst in O<sub>2</sub>- and N<sub>2</sub>-saturated 0.1 M KOH solutions at a scan rate of 10 mV s<sup>-1</sup>. (b) RDE polarization curves at different rotation rates in O<sub>2</sub>-saturated 0.1 M KOH solution at a scan rate of 10 mV s<sup>-1</sup>, inset: Koutecky-Levich plots. Reprinted with permission from ref. 50. Copyright 2015, John Wiley & Sons.

can be a potential candidate for rechargeable zinc-air batteries. Further analysis of discharging performance of this primary zinc-air battery is conducted at different constant current densities as in Figure 18(b). The cell voltages are stable during the whole discharge period of 20 h, except for a slight drop of approximately 0.05 V at the current density of 50 mA cm<sup>-2</sup>. This voltage drop can be attributed to the electrode polarization under high current density.

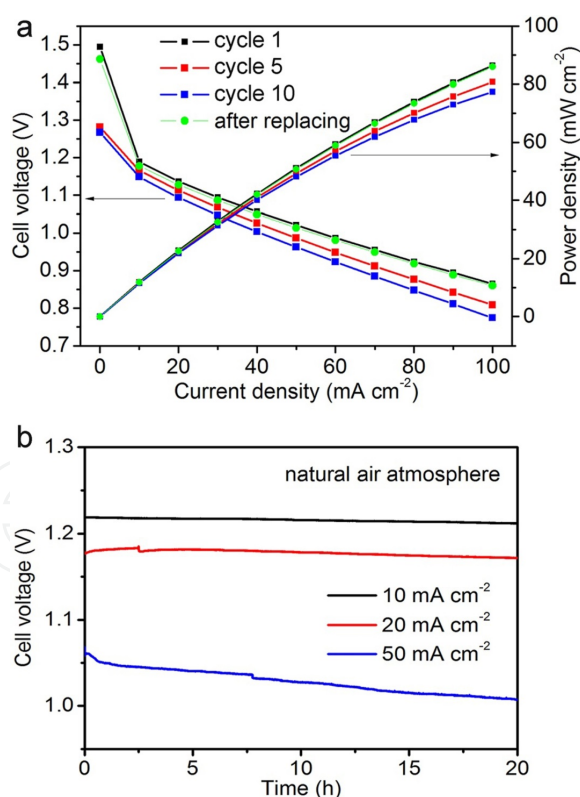


**Figure 18.** Performance of the primary zinc-air battery fabricated with an Ag<sub>50</sub>Cu<sub>50</sub> catalyst-based air cathode: a) Cell voltage and power density polarization curves of the battery over 10 cycles and the polarization curve after replacing Zn anode and electrolyte; b) discharge voltage curves at different current densities. Reprinted with permission from ref. 50. Copyright 2015, John Wiley & Sons.

Figure 19(a) shows the charge and discharge polarization curves of the secondary zinc-air battery. An abrupt polarization occurs when the current densities increase from 0 to  $10 \text{ mA cm}^{-2}$  because of the activation polarization and anode polarization [56]. However, once the zinc-air battery begins its function, the polarization exhibits a steady increase with varying current densities from  $10$  to  $100 \text{ mA cm}^{-2}$ . The charge–discharge voltage gap (i.e., the overpotential) at  $20 \text{ mA cm}^{-2}$  is  $0.9 \text{ V}$ , which is lower than that of  $\text{Co}_3\text{O}_4$ -based rechargeable zinc-air batteries [57,58]. The cycle performance with different cycle periods is shown in Figure 19(b). As seen in the bottom of Figure 19(b), the secondary zinc-air battery undergoes 100 charge and discharge cycles at  $20 \text{ mA cm}^{-2}$  with 20 min per step. The difference between the charge and discharge potentials is  $0.9 \text{ V}$ , and the overpotential shows no apparent fluctuation through all 100 cycles. The round-trip efficiency is up to 56.4%, which is a considerable improvement. A more violent charge and discharge cycle experiment is conducted with a cycle period of 4 h for the same rechargeable zinc-air battery after replacing the zinc anode and electrolyte. As shown in the top of Figure 19(b), the charge and discharge voltages are still stable even with the long cycle period; this result is comparable to the result of the tri-electrode rechargeable zinc-air battery.

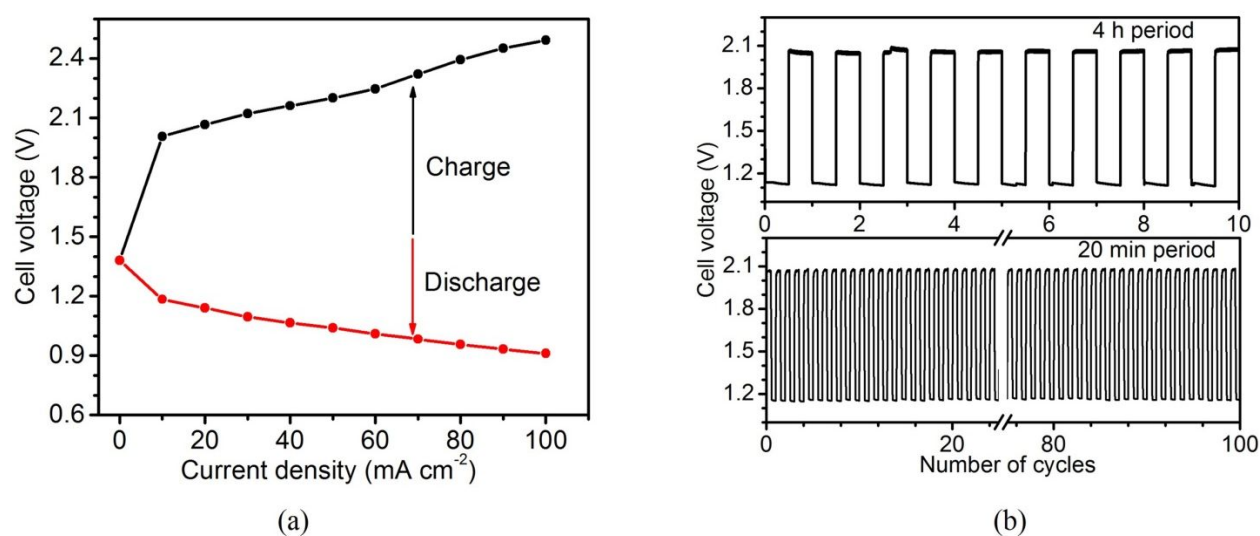


**Figure 19.** (a) Charge–discharge polarization curves for the rechargeable zinc air battery. b) Cycle performance for the rechargeable zinc-air battery at  $20 \text{ mA cm}^{-2}$  with a 20 min cycle period for 100 cycles and a 4 h cycle period for 40 h. Reprinted with permission from ref. 50. Copyright 2015, John Wiley & Sons.

## 4. Conclusions

Silver copper Ag–Cu nanoalloy particles have been investigated for prospective application as an electrocatalyst for oxygen reduction reaction in alkaline fuel cells and metal air battery systems. A holistic approach has been adopted incorporating density functional theory simulations along with synthesis of potential candidate compositions of Ag–Cu nanoalloys. Following conclusions can be drawn from this work:

1. Alloying of silver with copper significantly enhances the catalytic activity of silver for ORR. The enhancement of this catalytic activity is attributed to the modification of the surface electronic structure of the Ag–Cu nanoalloy catalyst.
2. Our DFT-based calculations confirm the rise of the d-band center of Ag–Cu nanoalloy catalyst toward Fermi level which in turn increases the adsorption strength of ORR intermediates on the catalyst surface during oxygen reduction. It has been well established that the optimum binding reaction intermediates such as O, OH, OOH are crucial for the fast kinetics of ORR.
3. The doping of a single Cu atom on the surface of 13 atom silver cluster improves the adsorption strength of ORR intermediates on the catalyst surface. We report that in case of 38 atom nanoalloy clusters, polyicosahedron (PIh) Ag<sub>32</sub>Cu<sub>6</sub> core-shell structure is found to be the most stable structure by genetic algorithm calculations. The most active catalytic site on the Ag<sub>32</sub>Cu<sub>6</sub> nanoalloy was also identified by our DFT calculations.
4. Ag–Cu nanoalloys have been successfully synthesized on Ni foams by pulse laser deposition as well as by chemical routes such as galvanic displacement and electrodeposition. Characterization of these nanoalloys by electron microscopy techniques (TEM, HRTEM, SEM) endorse the alloying of Ag and Cu atoms at the nanoscale.
5. Electrochemical characterization by rotating disc electrode methods (RDE) reveals the improvement of the ORR performance of the Ag–Cu nanoalloys due to the synergistic role of silver and copper in the Ag–Cu nanoalloys. Out of various compositions produced by PLD Ag<sub>50</sub>Cu<sub>50</sub> was observed to be the most active toward ORR in alkaline media. A twofold increase in limiting current density along with more positive onset potential was recorded in case of AgCu-10 nanoalloy compared to pure silver. We report four electron transfer pathway to be dominant during ORR in alkaline conditions on the surface of Ag–Cu nanoalloys.
6. Ni foam is reported here to be a suitable support for Ag–Cu nanoalloy catalysts which enables the elimination of binder-based carbon supports.

## 5. Future outlook

Ag–Cu nanoalloy catalysts offer an attractive alternative for the otherwise costly Pt-based alloys. The performance of these Ag–Cu nanoalloy catalysts was found to be reasonable while the stability in alkaline media is much superior compared to the Pt-based alloy catalysts. The realization of high energy density metal air batteries and alkaline fuel cells for stationary and mobile applications demand swift ORR kinetics at cathode which can be achieved by highly active silver-based nanoalloy electrocatalysts. Very few Ag-based Ag/transition metal nanoalloy electrocatalysts have been reported for ORR. Recently, the number of publications on silver-based nanoalloy electrocatalyst for ORR in alkaline media has been on the rise. DFT-based calculations show that the surface electronic structure of the nanoalloy catalyst is sensitive to doping. This opens the window for carrying out investigations on the ternary Ag–

Cu–M catalyst systems with different morphologies to further improve the catalytic activity. Moreover, the effect of support such as CNT, MWCNT, RGO is still to be investigated for the Ag–Cu nanoalloys. These advance catalyst supports have been previously reported to be highly beneficial for Ag-based systems. The highest amount of catalytic activity in Ag-based systems is reported in the Ag composites owing to the ensemble effect. Incorporation of Ag–Cu nanoalloys into composite structures can provide a big leap forward toward improving the catalytic activity of these nanoalloys. At present, the activity of silver nanoalloys in alkaline media is limited because of weak adsorption of ORR intermediates. Highly active silver nanoalloy compositions can be identified by DFT calculations which when combined with active supports can rival or even surpass commercial Pt/C in alkaline media. A universal approach incorporating first principle simulations and experimental analysis is pivotal for the realization of highly active and stable silver-based nanoalloy electrocatalysts for ORR in alkaline media.

## Acknowledgements

This study was supported by the National Natural Science Foundation of China (grant nos. 51271148 and 50971100), the Aeronautic Science Foundation Program of China (grant no. 2012ZF53073), the Science and Technology Innovation Fund of Western Metal Materials (grant no. XBCL-2-11) and the Doctoral Fund of Ministry of Education of China (grant no. 20136102110013).

## Author details

Adnan Qaseem, Fuyi Chen\* and Nan Zhang

\*Address all correspondence to: fuyichen@nwpu.edu.cn

State Key Laboratory of Solidification Processing, Northwestern Polytechnical University, Xian, China

## References

- [1] Nobuyuki Imanishi and Osamu Yamamoto. Rechargeable lithium–air batteries: characteristics and prospects. *Materials Today*. 2014;17(1):24–30. DOI: 10.1016/j.mattod.2013.12.004
- [2] Md. Arafat Rahman, Xiaojian Wang and Cuie Wen. A review of high energy density lithium–air battery technology. *Journal of Applied Electrochemistry*. 2014;44(1):5–22. DOI: 10.1007/s10800-013-0620-8



- [3] Nuria Garcia-Araez and Petr Novák. Critical aspects in the development of lithium–air batteries. *Journal of Solid State Electrochemistry*. July 2013; 17 (7):1793–1807. DOI: 10.1007/s10008-013-1999-1
- [4] Mark K. Debe. Electrocatalyst approaches and challenges for automotive fuel cells. *NATURE*. 2012;486(7401):43–51. DOI: 10.1038/nature11115
- [5] İbrahim Dincer and Calin Zamfirescu. Hydrogen and fuel cell systems. In: *Sustainable Energy Systems and Applications*. New York: Springer US; 2012. pp. 519–632. DOI: 10.1007/978-0-387-95861-3\_13
- [6] Marcel Pourbaix. *Atlas of Electrochemical Equilibria in Aqueous Solutions*. 2nd ed. US: National Association of Corrosion; 1974. 644 p. DOI: 0915567989
- [7] Edward McCafferty. Thermodynamics of Corrosion: Pourbaix Diagrams. In: Edward McCafferty, editor. *Introduction to Corrosion Science*. Springer New York; 2010. pp. 95–117. DOI: 10.1007/978-1-4419-0455-3\_6
- [8] J. K. Nørskov, J. Rossmeisl, A. Logadottir and L. Lindqvist. Origin of the overpotential for oxygen reduction at a fuel-cell cathode. *The Journal of Physical Chemistry B*. 2004;108 (46):17886–17892. DOI: DOI: 10.1021/jp047349j
- [9] Daojian Cheng, Xiangguo Qiu and Haiyan Yua. Enhancing oxygen reduction reaction activity of Pt-shelled catalysts via subsurface alloying. *Physical Chemistry Chemical Physics*. 2014;16(38): 20377–20381. DOI: 10.1039/c4cp02863e
- [10] Bongjin Simon Mun, Guofeng Wang, Philip N. Ross, Christopher A. Lucas, and Nenad M. Marković. Improved Oxygen Reduction Activity on Pt<sub>3</sub>Ni(111) via Increased Surface Site Availability. *Science*. 2007;315 (5811):493–497. DOI: 10.1126/science.1135941
- [11] Gongwei Wang, Bing Huang, Li Xiao, Zhandong Ren, Hao Chen, Deli Wang, Héctor D. Abruña, Juntao Lu, and Lin Zhuang. Pt Skin on AuCu Intermetallic Substrate: A Strategy to Maximize Pt Utilization for Fuel Cells. *Journal of the American Chemical Society (JACS)*. 2014;136(27):9643–9649. DOI: 10.1021/ja503315s
- [12] O A Petrii. Electrosynthesis of nanostructures and nanomaterials. *Russian Chemical Reviews*. 2015;84(2):159–193. DOI: 10.1070/RCR4438
- [13] J. Greeley, I. E. L. Stephens, A. S. Bondarenko, T. P. Johansson, H. A. Hansen, T. F. Jaramillo, J. Rossmeisl, I. Chorkendorff and J. K. Nørskov. Alloys of platinum and early transition metals as oxygen reduction electrocatalysts. *Nature Chemistry*. 2009;1:552–556. DOI: 10.1038/nchem.367
- [14] Hongliang Xin, Adam Holewinski, and Suljo Linic. Predictive Structure- Reactivity Models for Rapid Screening of Pt-Based Multimetallic Electrocatalysts for the Oxygen Reduction Reaction. *ACS Catalysis*. 2012;2:12–16. DOI: 10.1021/cs200462f
- [15] Mitsuru Wakisaka, Satoshi Mitsui, Yoshikazu Hirose, Katsura Kawashima, Hiroyuki Uchida, and Masahiro Watanabe. Electronic structures of Pt-Co and Pt-Ru alloys for



- CO-tolerant anode catalysts in polymer electrolyte fuel cells studied by EC-XPS. *The Journal of Physical Chemistry B*. 2006;110(46):23489–23496. DOI: 10.1021/jp0653510
- [16] B. Hammer and J.K. Nørskov. Theoretical surface science and catalysis—calculations and concepts. In: Bruce C. Gates, Helmut Knozinger, editors. *Advances in Catalysis*. 45th ed. Academic Press; 2000. pp. 71–129. DOI: 10.1016/S0360-0564(02)45013-4
- [17] Hongliang Xin, Adam Holewinski, Neil Schweitzer, Eranda Nikolla and Suljo Linic. Electronic structure engineering in heterogeneous catalysis: identifying novel alloy catalysts based on rapid screening for materials with desired electronic properties. *Topics in Catalysis*. 2012;55 (5-6):376–390. DOI: 10.1007/s11244-012-9794-2
- [18] Paul Sabatier. Hydrogénations et déshydrogénations par catalyse. *Berichte der deutschen chemischen Gesellschaft*. 1911;44(3):1984–2001. DOI: 10.1002/cber.19110440303
- [19] Ernest Yeager. Dioxygen electrocatalysis: mechanisms in relation to catalyst structure. *Journal of Molecular Catalysis*. 1986; 38(1–2):5–25. DOI:10.1016/0304-5102(86)87045-6
- [20] F. Bidault, D.J.L. Brett, P.H. Middleton and N.P. Brandon. Review of gas diffusion cathodes for alkaline fuel cells. *Journal of Power Sources*. 2009;187(1):39–48. DOI: 10.1016/j.jpowsour.2008.10.106
- [21] Vladimir Neburchilov, Haijiang Wang, Jonathan J. Martin and Wei Qu. A review on air cathodes for zinc–air fuel cells. *Journal of Power Sources*. 2010;195(5):1271–1291. DOI: 10.1016/j.jpowsour.2009.08.100
- [22] B.B. Blizanac, P.N. Ross and N.M. Markovic. Oxygen electroreduction on Ag(1 1 1): The pH effect. *Electrochimica Acta*. 2007;52 (6):2264–2271. DOI: doi:10.1016/j.electacta.2006.06.047
- [23] Adam Holewinski, Juan-Carlos Idrobo and Suljo Linic. High-performance Ag–Co alloy catalysts for electrochemical oxygen reduction. *Nature Chemistry*. 2014;6(9):828–834. DOI: 10.1038/nchem.2032
- [24] Lizhi Yuan, Luhua Jiang, Jing Liu, Zhangxun Xia, Suli Wang and Gongquan Sun. Facile synthesis of silver nanoparticles supported on three dimensional graphene oxide/carbon black composite and its application for oxygen reduction reaction. *Electrochimica Acta*. 2014;135:168–174. DOI: 10.1016/j.electacta.2014.04.137
- [25] Shin-Ae Park, Hankwon Lim and Yong-Tae Kim. Enhanced oxygen reduction reaction activity due to electronic effects between Ag and Mn<sub>3</sub>O<sub>4</sub> in alkaline media. *ACS Catalysis*. 2015;5(6):3995–4002. DOI: 10.1021/acscatal.5b00495
- [26] Junya Ohyama, Yui Okata, Noriyuki Watabe, Makoto Katagiri, Ayaka Nakamura, Hidekazu Arikawa, Ken-ichi Shimizu, Tatsuya Takeguchi, Wataru Ueda and Atsushi Satsuma. Oxygen reduction reaction over silver particles with various morphologies and surface chemical states. *Journal of Power Sources*. 2014;245(1):998–1004. DOI: doi:10.1016/j.jpowsour.2013.07.034

- [27] Raju P. Gupta. Lattice relaxation at a metal surface. *Physical Review B*. 1981;23(12): 6265–6270. DOI: <http://dx.doi.org/10.1103/PhysRevB.23.6265>
- [28] Weiyin Li and Fuyi Chen. A density functional theory study of structural, electronic, optical and magnetic properties of small Ag–Cu nanoalloys. *Journal of Nanoparticle Research*. 2013;15(7):1809. DOI: 10.1007/s11051-013-1809-9
- [29] F. Baletto, C. Mottet, and R. Ferrando. Growth simulations of silver shells on copper and palladium nanoclusters. *Physical Review B*. 2002;66(15):155420. DOI: <http://dx.doi.org/10.1103/PhysRevB.66.155420>
- [30] Roy L. Johnston. Evolving better nanoparticles: Genetic algorithms for optimising cluster geometries. *Dalton Transactions*. 2003;(22):4193–4207. DOI: 10.1039/B305686D
- [31] B. Delley. An all-electron numerical method for solving the local density functional for polyatomic molecules. *The Journal of Chemical Physics*. 1990;92(1):508. DOI: 10.1063/1.458452
- [32] B. Delley. From molecules to solids with the DMol3 approach. *The Journal of Chemical Physics*. (2000);113(18): 7756. DOI: 10.1063/1.1316015
- [33] J. Oviedo and R. E. Palmer. Amorphous structures of Cu, Ag, and Au nanoclusters from first principles calculations. *The Journal of Chemical Physics*. 2002;117(21):9548. DOI: 10.1063/1.1524154
- [34] Jonathan P. K. Doye and David J. Wales. Global minima for transition metal clusters described by Sutton–Chen potentials. *New Journal of Chemistry*. 1998;;22(7):733–744. DOI: 10.1039/A709249K
- [35] Wenqiang Ma, Fuyi Chen, Nan Zhang and Xiaoqiang Wu. Oxygen reduction reaction on Cu-doped Ag cluster for fuel-cell cathode. *Journal of Molecular Modeling*. 2014; 20:2454. DOI: 10.1007/s00894-014-2454-7
- [36] Kihyun Shin, Da Hye Kim, Sang Chul Yeo and Hyuck Mo Lee. Structural stability of AgCu bimetallic nanoparticles and their application as a catalyst: A DFT study. *Catalysis Today*. 2012;185(1):94–98. DOI: 10.1016/j.cattod.2011.09.022
- [37] Kihyun Shin, Da Hye Kim and Hyuck Mo Lee. Catalytic Characteristics of AgCu Bimetallic Nanoparticles in the Oxygen Reduction Reaction. *ChemSusChem*. 2013;6(6): 1044–1049. DOI: 10.1002/cssc.201201001
- [38] N. Zhang, F. Y. Chen and X.Q. Wu. Global optimization and oxygen dissociation on polyicosahedral Ag<sub>32</sub>Cu<sub>6</sub> core-shell cluster for alkaline fuel cells. *Scientific Reports* (2015) 5, Article number: 11984. DOI: 10.1038/srep11984
- [39] Rutger a. Van Santen and Matthew Neurock. Concepts in Theoretical Heterogeneous Catalytic Reactivity. *Catalysis Reviews: Science and Engineering*. 1995 ;37(4):557–698. DOI: 10.1080/01614949508006451
- [40] Waldemar Mróz, Bogusław Budner, Wojciech Tokarz, Piotr Piela and Michael L. Korwin-Pawłowski. Ultra-low-loading pulsed-laser-deposited platinum catalyst films for

- polymer electrolyte membrane fuel cells. *Journal of Power Sources*. 2015;273(1):885–893. DOI: 10.1016/j.jpowsour.2014.09.173
- [41] Sades Kumar Natarajan and Jean Hamelin. High-performance anode for polymer electrolyte membrane fuel cells by multiple-layer Pt sputter deposition. *Journal of Power Sources*. 2010;195(22):7574–7577. DOI: 10.1016/j.jpowsour.2010.06.027
- [42] Yachao Jin and Fuyi Chen. Facile preparation of Ag-Cu bifunctional electrocatalysts for zinc-air batteries. *Electrochimica Acta*. 2015;158:437–445. DOI: 10.1016/j.electacta.2015.01.151
- [43] M. J. Montenegro and M. Döbeli. Pulsed laser deposition of  $\text{La}_{0.6}\text{Ca}_{0.4}\text{CoO}_3$  (LCCO) films. A promising metal-oxide catalyst for air based batteries. *Physical Chemistry Chemical Physics*. 2002;4(12):2799–2805. DOI: 10.1039/B200120A
- [44] Shaomin Zhu, Zhu Chen, Bing Li, Drew Higgins, Haijiang Wang, Hui Li and Zhongwei Chen Nitrogen-doped carbon nanotubes as air cathode catalysts in zinc-air battery. *Electrochimica Acta*. 2011;56(14):5080–5084. DOI: 10.1016/j.electacta.2011.03.082
- [45] Yimin Lei, Fuyi Chen, Yachao Jin and Zongwen Liu. Ag-Cu nanoalloyed film as a high-performance cathode electrocatalytic material for zinc-air battery. *Nanoscale Research Letters*. 2015;10:197. DOI: 10.1186/s11671-015-0900-9
- [46] Xiaoqiang Wu, Fuyi Chen, Yachao Jin, Nan Zhang and Roy L. Johnston. Silver-copper nanoalloy catalyst layer for bifunctional air electrodes in alkaline media *ACS Application of Material Interfaces*. 2015;7(32):17782–17791. DOI: 10.1021/acsami.5b04061
- [47] Jia-Jun Han, Ning Li and Tian-Yun Zhang. Ag/C nanoparticles as an cathode catalyst for a zinc-air battery with a flowing alkaline electrolyte. *Journal of Power Sources*. 2009;193(2):885–889. DOI: 10.1016/j.jpowsour.2009.02.082
- [48] Ying Wang, Yu Li and Xiaojian Lu. Silver-molybdate electrocatalysts for oxygen reduction reaction in alkaline media. *Electrochemistry Communications*. 2012;20:171–174. DOI: 10.1016/j.elecom.2012.05.004
- [49] Yanguang Li, Ming Gong and Yongye Liang. Advanced zinc-air batteries based on high-performance hybrid electrocatalysts. *Nature Communications*. 2013;4:1805. DOI: 10.1038/ncomms2812
- [50] Yachao Jin, Fuyi Chen, Yimin Lei and Xiaoqiang Wu. A Silver-copper alloy as an oxygen reduction electrocatalyst for an advanced zinc-air battery. *Chemical Catalysis Catalytic Chemistry*. 2015;7(15):2377–2383. DOI: 10.1002/cctc.201500228
- [51] Sang Woo Han, Yunsoo Kim and Kwan Kim. Dodecanethiol-derivatized Au/Ag bimetallic nanoparticles: TEM, UV/VIS, XPS, and FTIR analysis. *Journal of Colloid and Interface Science*. 1998;208(1):272–278. DOI: 10.1006/jcis.1998.5812

- [52] Xianfeng You, Feng Chen, Jinlong Zhang and Masakazu Anpo. A novel deposition precipitation method for preparation of Ag-loaded titanium dioxide. *Catalysis Letters*. 2005;102(3-4):247–250. DOI: 10.1007/s10562-005-5863-5
- [53] C. C. Chusuei, M. A. Brookshier and D. W. Goodman. Correlation of relative X-ray photoelectron spectroscopy shake-up intensity with CuO particle size. *Langmuir*. 1999;15(8):2806–2808. DOI: 10.1021/la9815446
- [54] Po-Chieh Li, Chi-Chang Hu, Tai-Chou Lee, Wen-Sheng Chang and Tsin Hai Wang. Synthesis and characterization of carbon black/ manganese oxide air cathodes for zinc-air batteries. *Journal of Power Sources*. 2014;269:88–97. DOI: 10.1016/j.jpowsour.2014.06.108
- [55] Ting-Hao Yang, Shanmuganathan Venkatesan, Chien-Hung Lien, Jen-Lin Chang and Jyh-Myng Zen. Nafion/lead oxide–manganese oxide combined catalyst for use as a highly efficient alkaline air electrode in zinc–air battery. *Electrochimica Acta*. 2011;56(17):6205–6210. DOI: 10.1016/j.electacta.2011.03.094
- [56] Jia Wei Desmond Ng, Maureen Tang and Thomas F. Jaramillo. A carbon-free, precious-metal-free, high-performance O<sub>2</sub> electrode for regenerative fuel cells and metal–air batteries. *Energy & Environmental Science*. 2014;7(6):2017–2024. DOI: 10.1039/C3EE44059A
- [57] Dong Un Lee, Ja-Yeon Choi, Kun Feng, Hey Woong Park, and Zhongwei Chen. Advanced Extremely Durable 3D Bifunctional Air Electrodes for Rechargeable Zinc-Air Batteries. *Advanced Energy Materials*. 2014;4(6):1301389. DOI: 10.1002/aenm.201301389
- [58] Guojun Du, Xiaogang Liu, Yun Zong, T.S. Andy Hor, Aishui Yu and Zhaolin Liu. Co<sub>3</sub>O<sub>4</sub> nanoparticle-modified MnO<sub>2</sub> nanotube bifunctional oxygen cathode catalysts for rechargeable zinc–air batteries. *Nanoscale*. 2013;5(11):4657–4661. DOI: 10.1039/C3NR00300K

IntechOpen

